Journal of the Taiwan Institute of Chemical Engineers 185 (2026) 106665

Contents lists available at ScienceDirect

Journal of the Taiwan Institute of Chemical Engineers

journal homepage: www.journals.elsevier.com/journal-of-the-taiwan-institute-of-chemical-engineers

Hyaluronic acid-decorated Fe^{3+}-based metal-organic framework nanoparticles carrying juglone with dual-mode glutathione depletion to enhance tumor-targeted chemodynamic-chemo combination therapy

Yi-Ting Yeh [a], Wei-Jen Hsu [a,b], Tzu-Chen Lin [a], Ching-Ju Huang [a], I-Ju Liu [a], Shang-Hsiu Hu [c], De-Wei Lai [b,d,*], Wen-Hsuan Chiang [a,e,*]

[a] Department of Chemical Engineering, National Chung Hsing University, Taichung 402, Taiwan
[b] Department of Medical Research, Taichung Veterans General Hospital, Taichung 407, Taiwan
[c] Department of Biomedical Engineering and Environmental Sciences, National Tsing Hua University, Hsinchu 300, Taiwan
[d] Department of Health-Business Administration, Hungkuang University, Taichung 433, Taiwan
[e] i-Center for Advanced Science and Technology (iCAST), National Chung Hsing University, Taichung 402, Taiwan

ARTICLE INFO

Keywords:
Juglone
Metal-organic frameworks
Dual GSH depletion
Hyaluronic acid
Tumor-specific chemo/chemodynamic therapy

ABSTRACT

Background: Fenton reaction-driven chemodynamic therapy (CDT) is gaining attention as a novel method for destroying tumor cells by converting endogenous H_2O_2 into toxic hydroxyl radicals (•OH). Nevertheless, the non-specific tumor targeting of CDT reagents and the consumption of •OH by intracellular glutathione (GSH) remarkably diminish the antitumor effectiveness of CDT.

Methods: To achieve effective treatment of prostate cancer using tumor-specific chemodynamic-chemo combination therapy, the hyaluronic acid (HA)-decorated Fe^{3+}-based MIL-88B (HM) nanoparticles loaded with juglone, a phenolic compound, are developed.

Significant findings: The juglone@HM (JHM) nanoparticles exhibited an ultrahigh drug loading capacity (ca 35.1 wt%), uniform spindle-like shape, and excellent dispersion stability. The acidity/GSH-triggered disintegration of JHM nanoparticles efficiently accelerated the release of juglone molecules and Fe^{3+} ions. Additionally, the JHM nanoparticles displayed acidity-enhanced degradation of H_2O_2 into •OH via a Fenton or Fenton-like reaction as well as potent GSH consumption through juglone-mediated Michael addition and Fe^{3+}-elicited redox reaction. After uptake by TRAMP-C1 prostate cancer cells via CD44-mediated internalization, JHM nanoparticles depleted massive GSH and degraded H_2O_2 into •OH, leading to apoptosis and ferroptosis upon mitochondrial damage and lipid peroxidation. Importantly, the JHM nanoparticles prominently suppressed in vivo TRAMP-C1 tumor growth by GSH depletion-enhanced chemodynamic-chemo therapy.

1. Introduction

Over the past decade, chemodynamic therapy (CDT) has emerged as a promising cancer treatment strategy due to its high tumor selectivity, low systemic toxicity, and minimal invasiveness [1–5]. Through Fenton/Fenton-like reactions, multivalent metal ion pairs such as Cu^{+}/Cu^{2+}, Fe^{2+}/Fe^{3+}, and Mn^{2+}/Mn^{3+} can convert excess endogenous hydrogen peroxide (H_2O_2) within tumors to highly cytotoxic hydroxyl radicals (•OH) [1–5]. The produced •OH, the most active reactive oxygen species (ROS), can disturb intracellular redox balance and elicit permanent damage to cellular organelles, proteins, and DNA, ultimately leading to cancer cell death [6–8]. Also, intracellular massive •OH production has been demonstrated to damage lipid repair enzyme glutathione peroxidase 4 (GPX4) and promote lipid peroxidation (LPO), leading to ferroptosis, which plays a crucial synergistic role in CDT [6, 9–15]. Despite its promising potential, CDT still faces several significant challenges that restrict its clinical use. Although the H_2O_2 concentration (around 100 μM) in the tumor microenvironment (TME) is markedly higher than in normal tissues, it remains insufficient to support sustained •OH generation [16–18]. Furthermore, the intracellular excess glutathione (GSH) (2 to 10 mM), acting as a potent •OH scavenger, can maintain redox homeostasis in cancer cells and thereby largely decline the therapeutic efficacy of CDT [16–18]. Therefore, developing a CDT agent capable of depleting GSH is essential for enhancing the antitumor

* Corresponding authors.
E-mail addresses: deweilai123@vghtc.gov.tw (D.-W. Lai), whchiang@dragon.nchu.edu.tw (W.-H. Chiang).

https://doi.org/10.1016/j.jtice.2026.106665
Received 4 October 2025; Received in revised form 30 January 2026; Accepted 30 January 2026
Available online 4 February 2026

efficacy of CDT.

GSH depletion is typically achieved through two main approaches: conjugation with target molecules to form GS-X conjugates [19–21] and oxidation by metal ions (such as Fe^{3+}, Cu^{2+}, and Mn^{2+}) [22–25]. For example, Lin's group fabricated Fe^{3+}/naphthazarin metal-phenolic networks (FNP MPNs) using a simple one-step approach [20]. The FNP MPNs rapidly liberated naphthazarin and Fe^{3+} under GSH-rich acidic conditions, thus effectively consuming GSH via naphthazarin-mediated Michael addition and exerting Fe^{3+}-triggered Fenton reaction to generate substantial •OH to augment CDT effects. Moreover, a nanosized Cu^{2+}/catechol-based metal-organic framework (MOF) capable of oxidizing GSH into glutathione disulfide (GSSG) via Cu^{2+}-mediated redox reaction was developed by Liu et. al. to overcome cancer chemoresistance [25]. 5-hydroxy-1,4-naphthoquinone, a type of natural phenolic compound, also known as juglone, extracted from *Juglans regia*, has been recognized as a promising candidate for cancer therapy [26–28]. Several studies have demonstrated that juglone can deplete GSH via a Michael reaction between the thiol groups of GSH and the α,β-unsaturated ketone moiety of juglone [29–31]. Moreover, the anticancer effects of juglone are related to increased intracellular H_2O_2 production and its function as a natural inhibitor of peptidyl-prolyl cis-trans isomerase NIMA-interacting 1 (Pin1), an enzyme commonly overexpressed in cancer [32]. Nevertheless, the poor water solubility and lack of tumor targeting of juglone significantly hinder its applications in CDT-based cancer treatment. To address these issues, Lin's group developed Fe^{3+}-juglone nanoscale coordination polymers (FJNCPs) decorated with 1,2-distearoyl-sn-glycero-3-phosphoethanolamine conjugated polyethylene glycol (DSPE-PEG) [31]. The FJNCPs, as redox homeostasis disruptors, remarkably depleted intracellular GSH through Michael addition between juglone and GSH and Fe^{3+}-mediated GSH oxidation, as well as produced sufficient •OH to elicit potent ferroptosis and apoptosis. Furthermore, a magnetic nanoreactor, $CoFe_2O_4$@PALA-g-mPEG/juglone (CFO@PA-P/J), was fabricated by decorating magnetic $CoFe_2O_4$ (CFO) nanoparticles with a branched poly (α-lipoic acid) (PLA)-graft-mPEG loaded with juglone for highly efficient CDT [33]. The nanoreactor enabled the selective accumulation at tumor sites under the guidance of an external magnetic field, thus enhancing CDT-based antitumor potency. Despite some progress in the development of juglone delivery systems [28,31,33,34], few studies have focused on the fabrication of juglone delivery nanocarriers equipped with polysaccharide-driven tumor targeting and dual-mode GSH depletion for CDT-based tumor treatment. Furthermore, most juglone-loaded nanoparticles were fabricated using harsh hydrothermal methods that require high reaction temperatures and pressures [28] and/or dimethylformamide (DMF) as the reaction solvent [28,31,33]. DMF is classified as a Group 2A carcinogen by the International Agency for Research on Cancer, making these approaches unfavorable for clinical translation. Additionally, recent developments have led to the extensive growth of organic-inorganic materials for enhancing both catalytic performance and antibacterial activity [35–37]. Among them, MOFs composed of inorganic metal ions and organic bridging ligands have been extensively explored for gas storage, catalysis, sensors, water treatment, and membranes [38–41]. MOFs have demonstrated effectiveness in drug delivery by serving as carriers for nucleic acids, proteins, and small molecules [6–8,12,25,38–42].

To address the above issues and achieve effective treatment of prostate cancer using tumor-targeting and GSH depletion-enhanced chemodynamic-chemo combination therapy, juglone-carrying Fe^{3+}-based MIL-88B nanoparticles covalently conjugated with hyaluronic acid (HA), which is a natural polysaccharide capable of targeting CD44 receptor-overexpressed cancer cells, were fabricated under DMF-free and mild conditions. The attained juglone@HM (JHM) nanoparticles exhibited an ultrahigh drug loading capacity (ca 35.1 wt %), uniform spindle-like shape, and excellent dispersion stability in the serum-containing milieu. Through the acidity/GSH-triggered disintegration of JHM nanoparticles, the juglone molecules and Fe^{3+} ions were efficiently released. Also, the JHM nanoparticles prominently depleted GSH via juglone-mediated Michael addition and Fe^{3+}-elicited GSH oxidation, and effectively degraded H_2O_2 into •OH via Fenton/Fenton-like reaction in the acidic milieu. After uptake by TRAMP-C1 prostate cancer cells through CD44-mediated internalization, JHM nanoparticles depleted massive GSH and sufficiently degraded H_2O_2 into •OH, resulting in mitochondrial damage and LPO to promote apoptosis and ferroptosis. Notably, the JHM nanoparticles significantly suppressed in vivo TRAMP-C1 tumor growth without severe adverse effects. The caspase-3 and GPX4 staining of tumor sections further demonstrated that the JHM nanoparticle remarkably elicited apoptosis and ferroptosis by GSH depletion-enhanced chemodynamic-chemo combination therapy. Overall, this study highlights the potential of JHM nanoparticles as a promising platform for synergistic tumor therapy.

2. Experimental section

2.1. Materials and cell lines

Anhydrous iron (III) chloride (97 %) was obtained from SHOWA (Japan). HA sodium salt (Mw = 3000∼5000 g/mol, ≧ 91 %) was purchased from Glentham Life Science Ltd. (UK). 2-Aminoterephthalic acid (BDC-NH_2, 99 %), propidium (PI, 94 %), dichloro-dihydro-fluorescein diacetate (DCFH-DA, ≧ 97 %), IR780 (≧ 95 %), and Dulbecco′s Modified Eagle′s Medium (DMEM) were purchased from Sigma-Aldrich (USA). Terephthalic acid (THA, 98 %) and N-hydroxysuccinimide (NHS, 98 %) were obtained from Alfa Aesar (USA). Juglone (97 %) and 1,10-phenanthroline monohydrate (Phe, ≥99.5 %) were attained from Thermo Fisher Scientific. 5,5-dimethyl-1-pyrroline N-oxide (DMPO, 98 %) and N-(3-Dimethylaminopropyl)-N'-ethylcarbodiimide hydrochloride (EDC, 95 %) were purchased from Matrix Scientific. Fetal bovine serum (FBS) was purchased from Hyclone (USA). Hoechst 33,342 and BODIOY™581/591 C11 were obtained from Invitrogen (USA). The JC-1 assay kit was purchased from MedChemExpress (USA). 5,5′-dithiobis (2-nitrobenzoic acid) (DTNB) was purchased from Fluorochem (UK). 3-(4,5-Dimethylthiazol-2-yl)-2,5-diphenyltetrazolium bromide (MTT, > 98 %) was obtained from Alpha Biochemistry (Taiwan). 3,3′,5,5′-Tetramethylbenzidine (TMB, 99 %) was purchased from Acros Organics (USA). Calcein-AM was obtained from AAT Bioquest (USA). Anti-Glutathione peroxidase 4 (GPX4) antibodies (no. ab125066) were obtained from Abcam. TRAMP-C1 cells (murine prostate cancer cell line) were obtained from the Food Industry Research and Development Institute (Hsinchu City, Taiwan).

2.2. Synthesis of JHM nanoparticles

The JHM nanoparticles were prepared by the incorporation of juglone into HA-coated MIL-88B (HM) nanoparticles via hydrophobic and π-π stacking interactions. Firstly, $FeCl_3$ (8.9 mg) was dissolved in 5.0 mL of ethanol. Afterward, BDC-NH_2 in ethanol (5 mL, 4 mg/mL) was added dropwise to the $FeCl_3$ solution and stirred at 40 °C for 1.5 h. The resulting MIL-88B nanoparticles were purified by centrifugation (35 °C, 16,000 rpm, 20 min) and washed with 95 % ethanol and deionized water. Subsequently, the MIL-88 nanoparticle solution (1 mL, 1 mg/mL) was added to the aqueous solution containing HA segments (2.0 mg) whose carboxyl groups were activated by EDC and NHS, followed by stirring at 25 °C for 24 h to obtain the HM nanoparticles. To prepare the JHM nanoparticles, juglone in ethanol (1.0 mL, 0.5 mg/mL) was added to the HM nanoparticle solution (2.0 mL) and stirred at 25 °C for 24 h. Through centrifugation at 16,000 rpm, the JHM nanoparticles were collected and washed three times with 95 % ethanol, followed by dispersion in deionized water.

2.3. Characterization

The particle size and size distribution of MIL-88B, HM, and JHM

nanoparticles in aqueous solutions were measured by dynamic light scattering (DLS) using a Brookhaven BI-200SM goniometer equipped with a solid-state laser. The X-ray diffraction (XRD) patterns of MIL-88B, HM, and JHM nanoparticles were attained by a D8 Discover X-ray diffractometer (Bruker, Germany). The Litesizer 500 (Anton Paar, USA) was employed to determine the zeta potential of MIL-88B, HM, and JHM nanoparticles dispersed in 0.01 M NaCl aqueous solutions for 30 min. The morphology of various nanoparticles was observed by transmission electron microscope (TEM) (JEM-1400 FLASH, JEOL, Japan) and field emission scanning electron microscope (FE-SEM) (JSM-7800F, JEOL). X-ray energy dispersive spectroscopy (EDS) elemental mapping of JHM nanoparticles was acquired using TEM (JEM-F200, JEOL).

2.4. Determination of juglone loading efficiency and content

To quantify the juglone content in JHM nanoparticles, the supernatant was collected during the centrifugation step of the purification process. The absorbance of juglone in the supernatant at 424 nm was measured using a UV/Vis spectrophotometer (Hitachi U2900). The calibration curve for juglone loading characterization was obtained by the absorbance of juglone at various concentrations in ethanol/deionized water (v/v: 1/2) cosolvent (Fig. S1). The loading content (LC) and loading efficiency (LE) of juglone were estimated by the following formula:

$$\text{LC of juglone (wt\%)} = \frac{\text{Weight of juglone in feed} - \text{Weight of } \textit{juglone in the supernatant}}{\text{Total weight of JHM nanoparticles}} \times 100\ \%$$

$$\text{LE of juglone (\%)} = \frac{\text{Weight of juglone in feed} - \text{Weight of } \textit{juglone in the supernatant}}{\text{Weight of juglone in feed}} \times 100\ \%$$

2.5. In vitro juglone and Fe^{3+}liberation

To explore in vitro juglone release behavior, JHM nanoparticles were dispersed in pH 7.4 0.15 M saline solution and pH 5.0 acetate buffer with or without 10 mM GSH, respectively, at 37 °C. At the designated time points, the JHM nanoparticle solution was centrifuged at 25 °C (16,000 rpm for 10 min). The absorbance of the collected supernatant at 424 nm was measured using a UV/Vis spectrophotometer and compared with a calibration curve to quantify the amount of juglone released from the JHM nanoparticles. On the other hand, the in vitro Fe^{3+} release study was performed in the above manner. At the prescribed time, the JHM nanoparticle solution was centrifuged at 25 °C (16,000 rpm, 10 min). The supernatant was mixed with 1 mL of Vitamin C solution (40 mM) and 2 mL of Phe solution (2 mg/mL), and the mixture was reacted for 30 min. The absorbance of Fe^{2+}/Phe complexes at 510 nm was subsequently measured using a microplate reader (M200pro, Tecan). The absorbance was substituted into the pre-established calibration curve to calculate the amount of Fe^{3+} liberated from JHM nanoparticles. At least triplicate measurements of each sample were conducted and then averaged.

2.6. Fe^{2+} production and GSH depletion

The Phe assay was employed to verify the reduction of Fe^{3+} ions in JHM nanoparticles to Fe^{2+} by GSH. Briefly, JHM nanoparticles (50 μg/mL) were dispersed in pH 5.0 acetate buffer containing GSH (0.4 mM) and Phe (0.1 mg/mL), and incubated at 37 °C for 1 h. The mixture was then centrifuged at 25 °C, and the absorbance of the supernatant at 510 nm was determined using a microplate reader (M200pro, Tecan). For comparison, control experiments were performed using the following groups: JHM nanoparticles alone and $FeCl_3$ + GSH. On the other hand, the GSH-depleting capability of JHM nanoparticles was evaluated using the DTNB assay. In brief, 0.9 mL JHM nanoparticle solution (1 mg/mL) was mixed with 0.1 mL GSH solution (2 mM), and the mixture was incubated at 37 °C. At designated time points (10 min, 30 min, 1, 3, 6, and 24 h), the samples were centrifuged, and 0.5 mL of the supernatant was mixed with 0.5 mL of DTNB solution (0.2 mM) for 10 min. The absorption of the resulting solution was then measured using a microplate reader (M200pro, Tecan). For comparison, the GSH depletion induced by free juglone and HM nanoparticles was evaluated using a similar method, with the mixtures incubated at 37 °C for 30 min.

2.7. Catalytic performance

Electron spin resonance (ESR) measurement was used to detect the generation of •OH by DMPO. For the ESR spectrum of •OH, 100 μL of DMPO (1 M) was mixed with 1 mL solution containing HM nanoparticles or HM nanoparticles + H_2O_2 at pH 5.0, and then the mixture was transferred into a quartz capillary and measured on an EMX-plus spectrometer (Bruker, Germany). Furthermore, the catalytic activity of JHM nanoparticles for •OH generation at pH 7.4 and 5.0 was assessed by measuring the fluorescence intensity of 2-hydroxyterephthalic acid, formed from the reaction between THA and •OH. JHM nanoparticles (50 μg/mL) were dispersed in either pH 7.4 saline solution or pH 5.0 acetate buffer containing 1 mM H_2O_2 and 5 mM THA. The mixtures were incubated at 37 °C in the dark for 1 h, followed by centrifugation. Fluorescence intensity of the supernatant was measured at 420 nm using a fluorescence spectrophotometer (Hitachi F-2700). Moreover, the TMB assay was employed to evaluate the •OH generation of JHM nanoparticles at pH 7.4 and 5.0. JHM nanoparticles (50 μg/mL) were dispersed in aqueous solutions of pH 7.4 and 5.0 containing 1 mM H_2O_2 and 5 mM TMB and then incubated in the dark at 37 °C for different time intervals. The resulting solutions were centrifuged, and the absorption of the supernatant was measured using a microplate reader (M200pro, Tecan).

2.8. In vitro cellular uptake

The CD44-mediated internalization of IR780-labeled JHM (IJHM) nanoparticles by TRAMP-C1 cells was evaluated using fluorescence imaging. TRAMP-C1 cells (2×10^5 cells/well) were seeded onto 22 mm round glass coverslips placed in 6-well plates and cultured with IJHM nanoparticles (IR780 concentration: 20 μg/mL) at 37 °C for 1 h and 4 h, either in the presence or absence of free HA segments (10 mg/mL). After incubation, the cells were rinsed three times with HBSS and fixed with 4 % formaldehyde. The nuclei were then stained with Hoechst 33,342 for 5 min. Cellular images were acquired using a confocal laser scanning microscope (CLSM) (TCS SP5 II, Leica).

2.9. Intracellular Fe^{2+} generation and GSH depletion and •OH production

TRAMP-C1 cells seeded onto 22 mm round glass coverslips in 6-well plates (1.5×10^5 cells/well) were treated with juglone (20 μg/mL), HM (37.1 μg/mL), or JHM nanoparticles (juglone concentration: 20 μg/mL; HM concentration: 37.1 μg/mL) for 1.5 h. Afterward, the cells were incubated with RhoNox-1 (5 μM) at 37 °C for 30 min. A fluorescence microscope (DMI 6000B, Leica) was used to visualize intracellular RhoNox-1 fluorescence, with an excitation wavelength of 540 nm.

To evaluate the intracellular GSH consumption, TRAMP-C1 cells (2×10^5 cells/well) seeded into 6-well plates were incubated with juglone, HM, and JHM nanoparticles (juglone concentration: 20 μg/mL; HM concentration: 37.1 μg/mL), respectively, at 37 °C for 6 h. Subsequently, the treated cells were rinsed with PBS, detached using trypsin-EDTA, and centrifuged at 1200 rpm for 5 min. The resulting cell pellet was resuspended in 0.3 mL of RIPA buffer and subjected to a freeze-thaw cycle at -20 °C to achieve cell lysis. After lysis, the samples were centrifuged at 12,000 rpm for 25 min, and 100 μL of the supernatant was mixed with 50 μL of DTNB solution (1 mM). After 20 min, the absorbance of the resulting solution was then measured at 435 nm using a microplate reader (M200pro, Tecan). All measurements were performed in triplicate and averaged. The intracellular GSH level was calculated using the following formula:

$$\text{Intracellular GSH level } (\%) = \frac{\textit{Absorbance of experimental group}}{\textit{Absorbance of control group}} \times 100$$

To assess the intracellular •OH production, TRAMP-C1 cells were seeded onto 22 mm round glass coverslips in 6-well plates at a density of 1.5×10^5 cells per well and then treated for 1.5 h with juglone (20 μg/mL), HM (37.1 μg/mL), or JHM nanoparticles (juglone concentration: 20 μg/mL; HM concentration: 37.1 μg/mL). Next, the cells were rinsed with HBSS and then incubated with DCFH-DA (5 μM) at 37 °C for 30 min, washed with HBSS, and fixed with 4 % formaldehyde. Fluorescence images were acquired using a CLSM (TCS SP5 II, Leica).

2.10. Intracellular LPO determination

TRAMP-C1 cells (1.5×10^5/well) attached in a 6-well plate were incubated with juglone (20 μg/mL), HM (37.1 μg/mL), or JHM nanoparticles (juglone concentration: 20 μg/mL; HM concentration: 37.1 μg/mL), respectively, at 37 °C for 1.5 h. After eliminating the culture medium, the cells were incubated with 5 μM BODIPY™ 581/591 C11 for 30 min, then rinsed with HBSS and fixed with 4 % formaldehyde. LPO was visualized using fluorescence microscopy (DMI 6000B, Leica) with an excitation wavelength of 514 nm for BODIPY detection.

2.11. Mitochondrial membrane potential (MMP) analysis

Mitochondrial membrane depolarization was assessed using the JC-1 MMP detection kit. TRAMP-C1 cells (1.5×10^5 cells/well) seeded in 6-well plates were incubated with juglone (20 μg/mL), HM (37.1 μg/mL), or JHM nanoparticles (juglone concentration: 20 μg/mL; HM concentration: 37.1 μg/mL) at 37 °C for 1.5 h. After eliminating the culture medium, the cells were stained with JC-1 (2 μM) for 30 min and then fixed with 4 % formaldehyde. Fluorescence images were acquired using a fluorescence microscope (DMI 6000B, Leica) with excitation wavelengths of 488 nm for JC-1 monomers and 514 nm for JC-1 aggregates.

2.12. In vitroanticancer potency of chemodynamic-chemo therapy

TRAMP-C1 cells (1×10^4 cells/well) seeded in 96-well plates were incubated with DMEM containing juglone, HM, or JHM nanoparticles of various concentrations for 24 h. Subsequently, the culture medium was removed, and 100 μL of MTT solution (0.25 mg/mL) was added to each well, followed by incubation for 3 h. The supernatant was then removed, and DMSO was added to dissolve the resulting formazan crystals. The absorbance was measured at 570 nm using a microplate reader (M200pro, Tecan).

The anticancer efficacy of chemodynamic-chemo therapy mediated by JHM nanoparticles was further assessed using calcein-AM/PI live/dead cell staining in TRAMP-C1 cells. TRAMP-C1 cells (1.5×10^5 cells/well) seeded in 6-well plates were treated with juglone (20 μg/mL), HM (37.1 μg/mL), or JHM nanoparticles of various concentrations. After treatment, cells were washed with HBSS and stained with calcein-AM (2 μM) for 45 min, followed by staining with PI (4.5 μM) for 15 min. Fluorescence images were acquired using a fluorescence microscope (DMI 6000B, Leica).

2.13. Animals and tumor model

Male C57BL/6 J mice (6~8 weeks old) were acquired from the National Laboratory Animal Center (Taiwan) and cared for according to the Guidance Suggestions for the Care and Use of Laboratory Animals, approved by the Administrative Committee on Chang Bing Show Chwan Memorial Hospital (Taiwan) (IACUC Approval No: 113,006). To establish a tumor model, 100 μL of PBS containing 8×10^6 TRAMP-C1 cells was subcutaneously injected into the right hind leg of mice. Tumor volume (V) was calculated using the formula: $V = (L \times W^2)/2$, where W represents the tumor's widest dimension, and L denotes its longest dimension.

2.14. In vivo imaging and biodistribution

The hemocompatibility of JHM nanoparticles was assessed using a hemolysis assay. Mouse blood was collected, and red blood cells were isolated by centrifugation. A 2 % red blood cell suspension was incubated with various concentrations of JHM nanoparticles for 1 h, and the hemolysis rate was quantified by measuring the absorbance at 570 nm. Red blood cells incubated in deionized water and in 0.9 % saline solution served as the positive and negative controls, respectively. Once tumor volumes reached 90–120 mm^3, mice were randomly divided into three groups ($n = 3$) and intravenously injected with PBS, free IR780, or IJHM nanoparticles (100 μL) at an IR780 dosage of 1.0 mg/kg. Fluorescence signals of IR780 (excitation: 745 nm; emission: 810 nm) were captured at 2, 4, 6, and 24 h post-injection using an IVIS imaging system (Xtreme II imaging system, Bruker). The treated mice were sacrificed by CO_2 euthanasia at 24 h post-injection, and the major organs and tumors were collected for imaging by IVIS.

2.15. In vivo tumor growth suppression

When tumor volumes reached approximately 90–120 mm^3, mice were randomly divided into four groups ($n = 5$ per group): (i) PBS, (ii) juglone, (iii) HM nanoparticles, and (iv) JHM nanoparticles. Each group received an intravenous injection of the corresponding formulation (100 μL) at a dose of 1.0 mg juglone/kg and/or 1.86 mg HM nanoparticles/kg. Treatments were administered in three doses on days 0, 3, and 6. Tumor

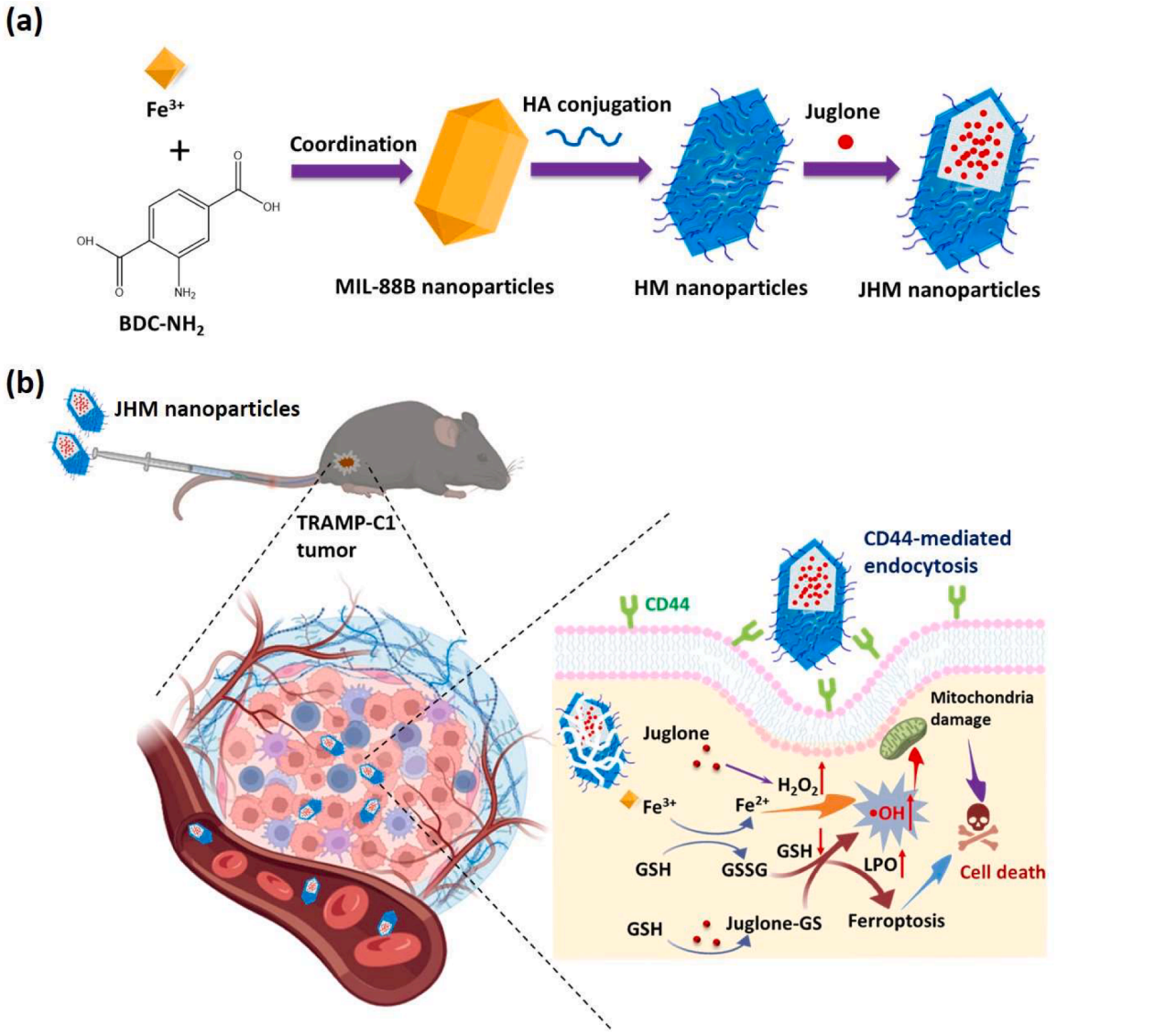

Scheme 1. (a) Synthetic tactics and coordination architecture of JHM nanoparticles. (b) The antitumor mechanism of JHM nanoparticles: CD44-mediated endocytosis, acidity/GSH-triggered disintegration of JHM nanoparticles to release juglone and Fe^{3+}, dual-model Fe^{3+}/juglone-driven GSH depletion, juglone-elicited H_2O_2 generation, Fe^{3+}/Fe^{2+}-mediated Fenton reaction to degrade H_2O_2 into •OH, •OH-induced mitochondria damage, and •OH-triggered LPO and ferroptosis, causing cell death.

volume and body weight were recorded every two days for up to 14 days post-treatment. After the treatment, all mice were euthanized, and major organs, including the heart, liver, spleen, lung, and kidney, were collected, and tumors were then photographed and weighed. Tumor sections of appropriate size were stained with hematoxylin and eosin (H&E), anti-caspase-3 antibodies, and anti-GPX4 antibodies, respectively, and examined using a digital microscope. Additionally, sections of major organs were stained with H&E and analyzed using the same instrument.

2.16. Statistical analysis

The data are presented as mean ± standard deviation. Two-way ANOVA analysis was performed using GraphPad Prism software to determine the differences among the groups. ns $p > 0.05$, *$p < 0.05$, **$p < 0.01$, ***$p < 0.001$, ****$p < 0.0001$.

3. Results and discussion

3.1. Preparation and characterization of JHM nanoparticles

The synthetic protocol of JHM nanoparticles is revealed in Scheme 1a. Through the coordination of $FeCl_3$ with BDC-NH_2 ligands, the MIL-88B nanoparticles were attained and characterized by DLS to have a mean hydrodynamic diameter of ca. 120 nm (Fig. 1a and Table 1). As presented in the XRD curves (Fig. 1b), the MIL-88B nanoparticles showed the diffraction peaks at 9.2°, 10.3°, 13.1°, 16.7°, 18.6°, and 20.8° similar to the simulated MIL-88B, thereby verifying the successful synthesis of MIL-88B nanoparticles with well-defined crystalline structure. The TEM and SEM images in Fig. S2 revealed that the MIL-88 nanoparticles had a spindle-like form as reported elsewhere [43,44]. To equip MIL-88 nanoparticles with CD44-targeting capability, the HA segments were covalently conjugated with MIL-88 nanoparticles upon EDC/NHS-mediated amidation. After being decorated with HA segments, the MIL-88 nanoparticles showed an enlargement in the mean hydrodynamic diameter from 120 to 140.4 nm (Fig. 1a and Table 1) and

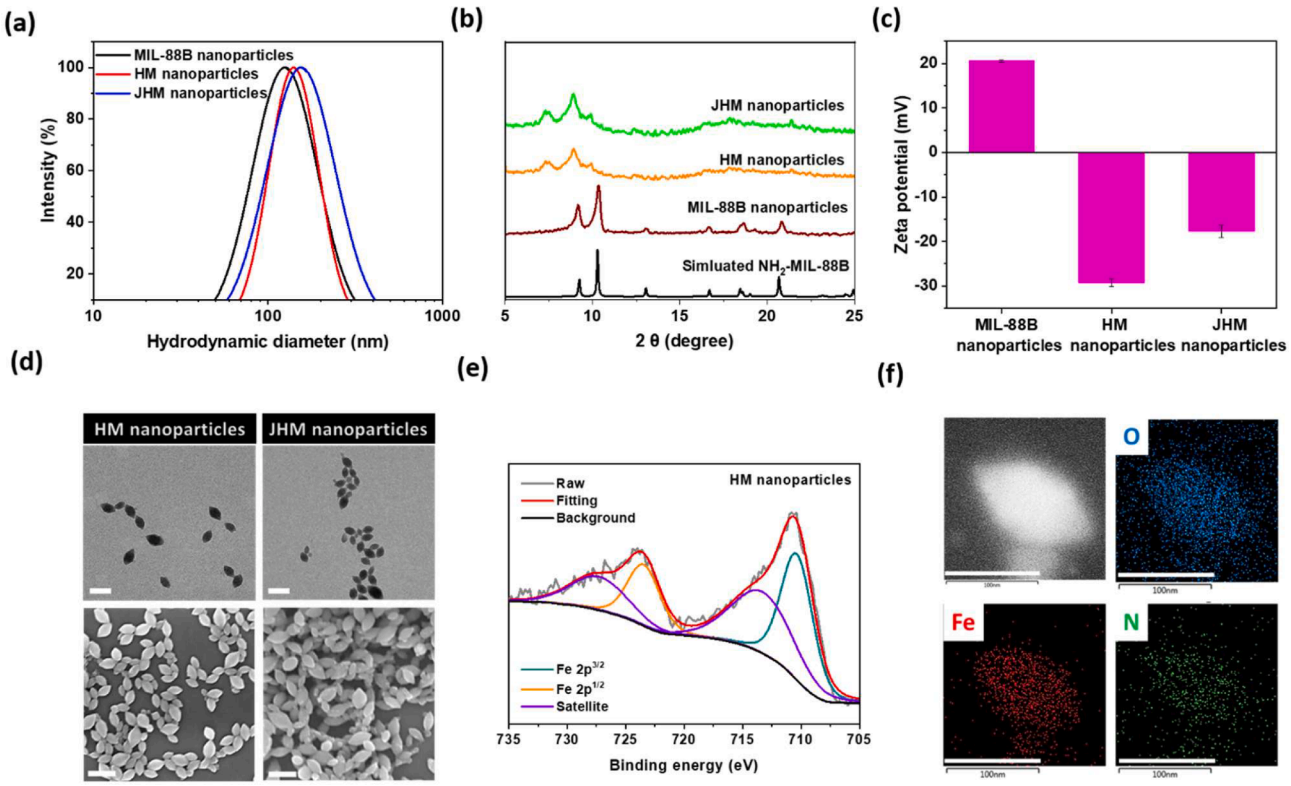

Fig. 1. (a) DLS particle size distribution of MIL-88B nanoparticles, HM nanoparticles, and JHM nanoparticles dispersed in deionized water. (b) XRD patterns of MIL-88B nanoparticles, HM nanoparticles, and JHM nanoparticles. (c) Zeta potential of MIL-88B nanoparticles, HM nanoparticles, and JHM nanoparticles dispersed in 0.01 M NaCl aqueous solution. (d) TEM (top) and SEM (bottom) images of HM nanoparticles and JHM nanoparticles. Scale bar: 200 nm (e) Fe 2p XPS spectra of HM nanoparticles. (f) Corresponding elements O, Fe, and N mapping images of JHM nanoparticles. The scale bar was 100 nm.

Table 1
Particle size and drug loading data of various nanoparticles.

Sample	Mean hydrodynamic diameter (nm)	PDI	LC (wt %)	LE (%)
MIL-88B nanoparticles	120.0 ± 1.9	0.23 ± 0.03	-	-
HM nanoparticles	140.4 ± 4.0	0.20 ± 0.03	-	-
JHM nanoparticles	158.9 ± 4.7	0.23 ± 0.02	35.1 ± 2.5	69.1 ± 1.5

a significant conversion in the zeta potential from +20.6 to -29.3 mV (Fig. 1c) due to the presence of carboxylic acid-rich HA surface coating. Note that the attained HM nanoparticles retained intact spindle-like shape and crystalline structure similar to MIL-88B nanoparticles (Fig. 1b and d). Furthermore, the Fe 2p XPS spectrum of HM nanoparticles exhibited binding energy peaks at 710.6 and 714.0 eV, corresponding to the Fe $2p^{3/2}$ main peak and its Fe^{3+} satellite, as well as peaks at 723.6 and 727.8 eV assigned to the Fe $2p^{1/2}$ main peak and its Fe^{3+} satellite (Fig. 1e). These results, consistent with those of MIL-88B nanoparticles (Fig. S3), confirm that HA surface modification did not alter the valance status of Fe^{3+}. Unlike the significant particle size increase observed in MIL-88B nanoparticles after 24 h in pH 7.4 0.9 % saline solution due to severe inter-particle flocculation (Fig. S4a), the HM nanoparticles showed a slightly increased particle size under the same conditions for 24 h (Fig. S4b). This indicates that a sufficient coverage of hydrophilic HA segments on the surfaces of HM nanoparticles is crucial for improving their colloidal stability and preventing inter-particle aggregation.

Through the coordination and π-π stacking interaction of juglone molecules with ferric ions and BDC-NH_2 of HM nanoparticles, respectively, followed by surface modification with HA, the JHM nanoparticles were gained. The JHM nanoparticles exhibited a mean hydrodynamic diameter of ca 158.9 nm and zeta potential of -17.8 mV (Table 1, Fig. 1a and c). Notably, the XRD pattern of JHM nanoparticles closely resembled that of HM nanoparticles, demonstrating that the JHM nanoparticles maintained an undamaged crystalline architecture. Additionally, TEM and SEM images (Fig. 1d) revealed that JHM nanoparticles displayed a spindle-like shape, similar to both HM and MIL-88B nanoparticles. The homogeneous distributions of O, N, and Fe observed in elemental mappings confirm the presence of juglone and Fe in JHM nanoparticles (Fig. 1f), validating the successful synthesis of JHM nanoparticles as designed. The drug loading content of JHM nanoparticles was estimated to be 35.1 wt % (Table 1). As presented in Figs. S5a and 2a, the JHM nanoparticles dispersed in 10 % FBS-containing DMEM or pH 7.4 0.9 % saline solution for 24 h maintained nearly unchanged particle size. Moreover, no significant variation in the particle size of JHM nanoparticles stored in deionized water at 4 °C was observed over 21 days (Fig. S5b). These results signify the robust colloidal stability of JHM nanoparticles.

As presented in Fig. 2a and b, compared to the virtually unvaried particle size of JHM nanoparticles dispersed in a pH 7.4 saline solution for 24 h, the particle size of JHM nanoparticles in a pH 5.0 acetate buffer was somewhat increased from 158.9 nm to 231 nm over 24 h. This could be attributed to that the increased acidity promotes the protonation of the carboxylic acid groups in BDC-NH_2, somewhat disrupting the coordination between Fe^{3+} ions and BDC-NH_2 ligands, which leads to the instability and swelling of JHM nanoparticles in acidic environments. Such an acidity-elicited instability of Fe-based MOF nanoparticles was also reported elsewhere [45,46]. Notably, after being dispersed in a pH 5.0 acetate buffer containing 10.0 mM GSH for 12 h, the JHM nanoparticles showed an appreciably enlarged particle size over 2000 nm (Fig. 2c). As shown in the TEM images (Fig. 2d), the structure of JHM

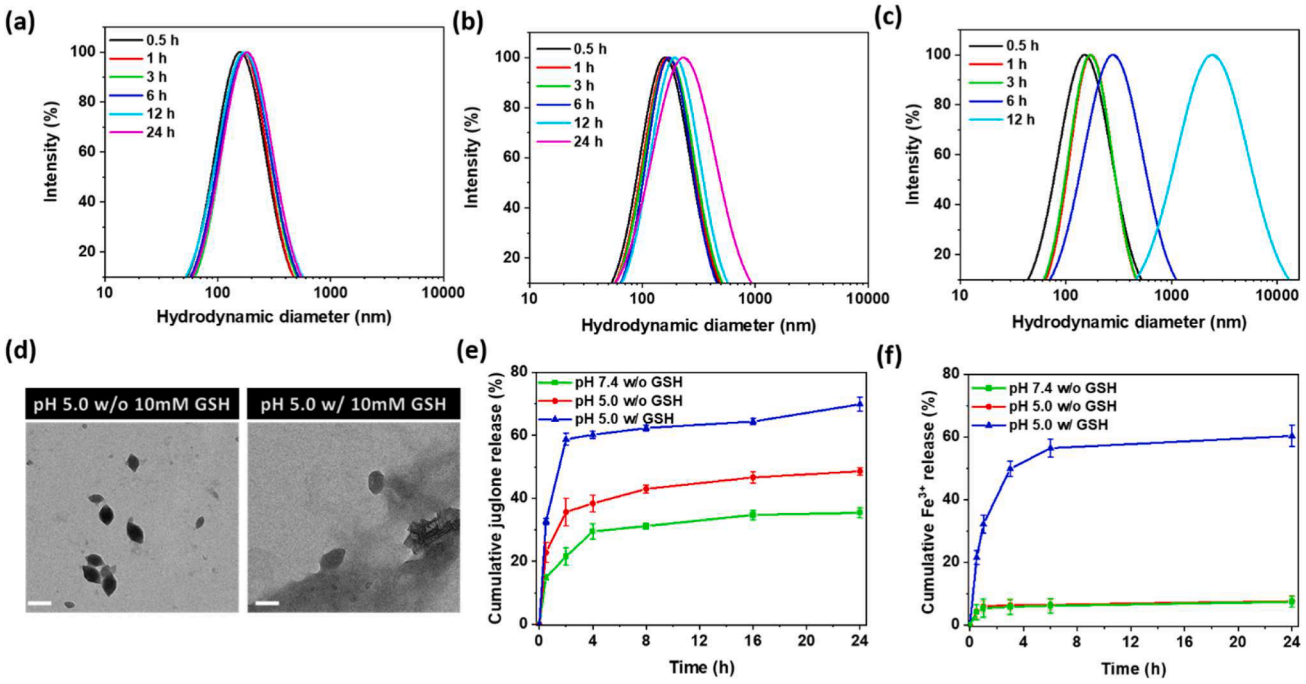

Fig. 2. DLS particle size distributions of JHM nanoparticles dispersed in (a) pH 7.4 0.9 % saline solution, (b) pH 5.0 acetate buffer, or (c) pH 5.0 acetate buffer containing 10.0 mM GSH for different time intervals. (d) TEM images of JHM nanoparticles incubated in a pH 5.0 acetate buffer with or without GSH for 12 h. Scale bar: 200 nm. Cumulative release of (e) juglone and (f) Fe^{3+} from JHM nanoparticles in pH 7.4 and pH 5.0 solution, and 10.0 mM GSH-containing pH 5.0 solution, respectively, at 37 °C.

nanoparticles exhibited remarkable structural distortion and collapse after incubation under GSH-rich acidic conditions for 12 h, while the morphology of most JHM nanoparticles maintained its original shape in a GSH-free pH 5.0 milieu for 12 h. These findings suggest that the GSH-mediated Fe^{3+} reduction could efficiently facilitate the disintegration of JHM nanoparticles under weakly acidic conditions by largely destroying the coordination between Fe^{3+} ions and BDC-NH_2 ligands. On the other hand, when the environment was changed from pH 7.4 saline solution to GSH-containing pH 5.0 acetate buffer, the cumulative release of juglone from JHM nanoparticles appreciably increased from 35.4 to 69.9 % over 24 h (Fig. 2e). The acidity/GSH-enhanced Fe^{3+} release from JHM nanoparticles was also attained (Fig. 2f). Based on the above results, it can be demonstrated that the acidity/GSH-triggered fragmentation of JHM nanoparticles effectively promotes juglone and Fe^{3+} release, being beneficial to realizing tumor-specific chemodynamic-chemo therapy.

3.2. *Dual-mode GSH depletion and Fenton reaction-mediated •OH production*

Because of the abundant Fe^{3+} and juglone of JHM nanoparticles, it was assumed that the JHM nanoparticle could consume GSH via Fe^{3+}-mediated redox reaction and juglone-involved Michael addition. To evaluate the GSH-oxidizing ability of JHM nanoparticles through Fe^{3+} reduction, Phe, a chelator with strong affinity for divalent metal ions, was used to detect Fe^{2+} ions generated from JHM nanoparticles upon treatment with GSH. Upon mixing the JHM nanoparticle solution with Phe and GSH, a distinct absorption peak at 512 nm was observed (Fig. 3a), accompanied by a noticeable red coloration, similar to that attained in $FeCl_3$ solution subjected to the same treatment. In contrast, in the absence of GSH, the aqueous solution containing JHM nanoparticles and Phe exhibited no significant absorption peak. These findings suggest that the JHM nanoparticles could generate Fe^{2+} ions by Fe^{3+}-induced GSH oxidation, which subsequently form orange-colored complexes with Phe. It should be highlighted that Fe^{2+} ions exhibit better Fenton reaction-based catalytic efficiency compared to Fe^{3+} ions [47]. Next, the GSH-depleting capability of JHM nanoparticles was further assessed by the DTNB assay [47,48]. As shown in Fig. 3b, the DTNB solution mixed with GSH alone, serving as an important control, exhibited a characteristic peak at 412 nm. In contrast, the GSH solution treated with juglone molecules, HM nanoparticles, or JHM nanoparticles for 30 min, followed by mixing with DTNB solution, showed appreciably decreased absorbance at 412 nm, particularly JHM nanoparticles. Moreover, when the reaction time of the GSH and JHM nanoparticles was prolonged from 10 min to 24 h, the absorbance of the GSH-treated DTNB solution gradually declined (Fig. 3c). A similar result was also attained in the GSH + juglone group (Fig. S6). These results demonstrate that JHM nanoparticles could maximize GSH consumption through juglone-mediated Michael addition combined with Fe^{3+}-driven oxidation. The ESR spectrometer was employed to detect •OH by using DMPO as a trapping probe [49,50]. A typical 1:2:2:1 four-line signal of •OH was observed in the HM nanoparticles + H_2O_2 group (Fig. 3d), indicating the •OH production driven by the HM nanoparticle-mediated Fenton reaction. Furthermore, the ability of JHM nanoparticles to generate •OH via the Fenton reaction was assessed using THA as a probe, which is oxidized to oxTHA with a characteristic fluorescence at 430 nm in the presence of •OH. In the absence of JHM nanoparticles, no significant fluorescence was observed in the THA + H_2O_2 groups at pH 7.4 or 5.0 (Fig. 3e). Notably, the fluorescence intensity of the oxidized THA in the JHM nanoparticles + THA + H_2O_2 groups was considerably enhanced as the solution pH was adjusted from 7.4 to 5.0. TMB was further utilized as a probe, which is oxidized to oxTMB with a characteristic absorption at 650 nm in the presence of •OH. Corresponding to the above results, the appreciably increased absorbance of oxTMB in the JHM nanoparticles + TMB + H_2O_2 groups at pH 5.0 compared to at pH 7.4 was attained (Fig. 3f). Collectively, these findings confirm that JHM nanoparticles efficiently convert H_2O_2 into •OH via an acidity-augmented Fenton reaction, promoting the oxidation of both TMB and THA. Some MOF-based nanozymes capable of showing acidity-enhanced Fenton reaction have also been reported elsewhere

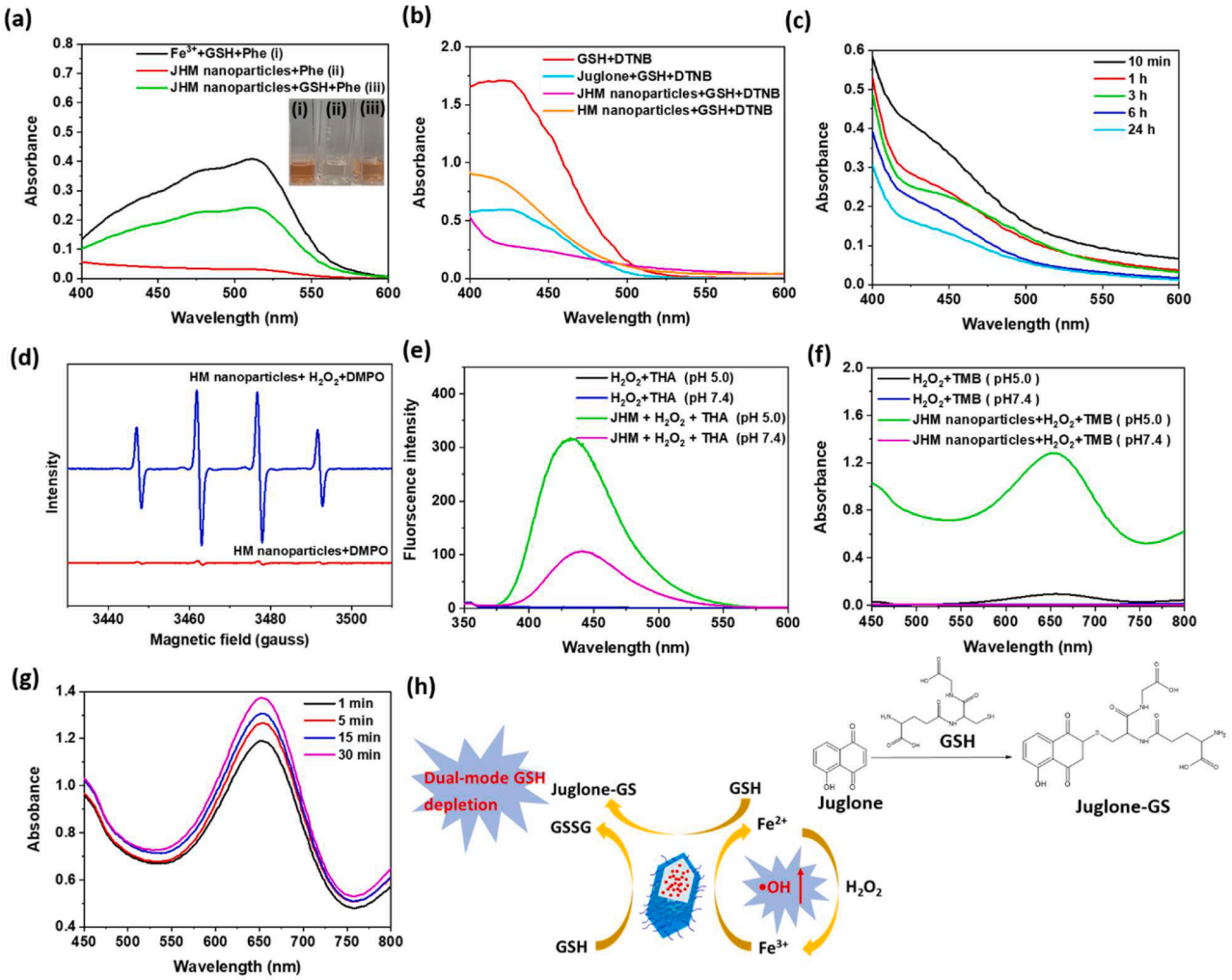

Fig. 3. (a) UV/Vis absorption of Phe subjected to various treatments. Inset: photos of the corresponding samples. (b) UV/Vis absorption of DTNB molecules mixed with GSH solution pretreated with different formulations. (c) UV/Vis absorption of DTNB molecules mixed with GSH solution pretreated with JHM nanoparticles for various time intervals. (d) ESR spectra of different reaction systems using DMPO as the trapping agent. (e) Fluorescence spectra of THA treated with the aqueous solution of JHM nanoparticles at pH 7.4 and 5.0 in the presence or absence of H_2O_2 for 1 h. (f) UV/Vis absorption of TMB treated with the aqueous solution of JHM nanoparticles at pH 7.4 and 5.0 in the presence or absence of H_2O_2. (g) UV/Vis absorption of TMB treated with the aqueous solution of JHM nanoparticles at pH 5.0 in the presence of H_2O_2 for different time intervals. (h) Schematic illustration of the mechanism for •OH generation and dual-mode GSH consumption driven by the JHM nanoparticles.

[51,52]. On the other hand, it was found that the absorbance of oxTMB in the JHM nanoparticles + TMB + H_2O_2 group at pH 5.0 increased gradually with prolonging reaction time from 1 to 30 min (Fig. 3g), indicating the production of more •OH from JHM nanoparticle-mediated Fenton/Fenton-like reaction. Based on these results, the developed JHM nanoparticles exhibited dual-mode GSH exhaustion and acidity-enhanced Fenton reaction activity (Fig. 3h), beneficially boosting the anticancer efficacy of CDT.

3.3. *In vitro cellular uptake and intracellular GSH depletion and •OH generation*

Increasing studies have demonstrated that HA-coated therapeutic nanoparticles efficiently target overexpressed CD44 receptors on cancer cells, promoting intracellular drug transport [53,54]. Therefore, assessing the CD44-targeting capability of JHM nanoparticles through in vitro cellular uptake studies was crucial. Since JHM nanoparticles lack inherent fluorescence, the fluorescent dye IR780 was encapsulated into JHM nanoparticles to form IR780@JHM (IJHM) nanoparticles for fluorescence imaging. Cellular internalization of IJHM nanoparticles by CD44-overexpressing TRAMP-C1 prostate cancer cells was analyzed using CLSM. With the co-incubation time being prolonged from 1 to 4 h, TRAMP-C1 cells treated with IJHM nanoparticles showed remarkably enhanced IR780 fluorescence signals compared to those co-incubated with both IJHM nanoparticles and free HA segments (Fig. 4a). These results strongly indicate that IJHM nanoparticles could be efficiently internalized by TRAMP-C1 cells via CD44 receptor-mediated endocytosis, while extra free HA segments compete with IJHM nanoparticles for CD44 binding sites, thereby hindering the uptake of nanoparticles by TRAMP-C1 cells. Notably, as presented in the RhoNox-1 staining images (Fig. 4b), in contrast to the weak fluorescence observed in TRAMP-C1 cells treated with PBS (control) or free juglone, cells incubated with HM or JHM nanoparticles exhibited bright orange fluorescence. This suggests that the intracellular acidity/GSH-driven fragmentation of these nanoparticles could efficiently release Fe^{3+} ions, which are then reduced to Fe^{2+} ions by GSH. These observations are consistent with the above results regarding the acidity/GSH-elicited Fe^{3+} release from JHM nanoparticles (Fig. 2f) and GSH-triggered Fe^{3+} reduction as shown by the Phe assay (Fig. 3a).

Considering the demonstrated dual-mode GSH depletion capability shown in Fig. 3b, the ability of JHM nanoparticles to consume intracellular GSH was further assessed using the DTNB assay. As shown in

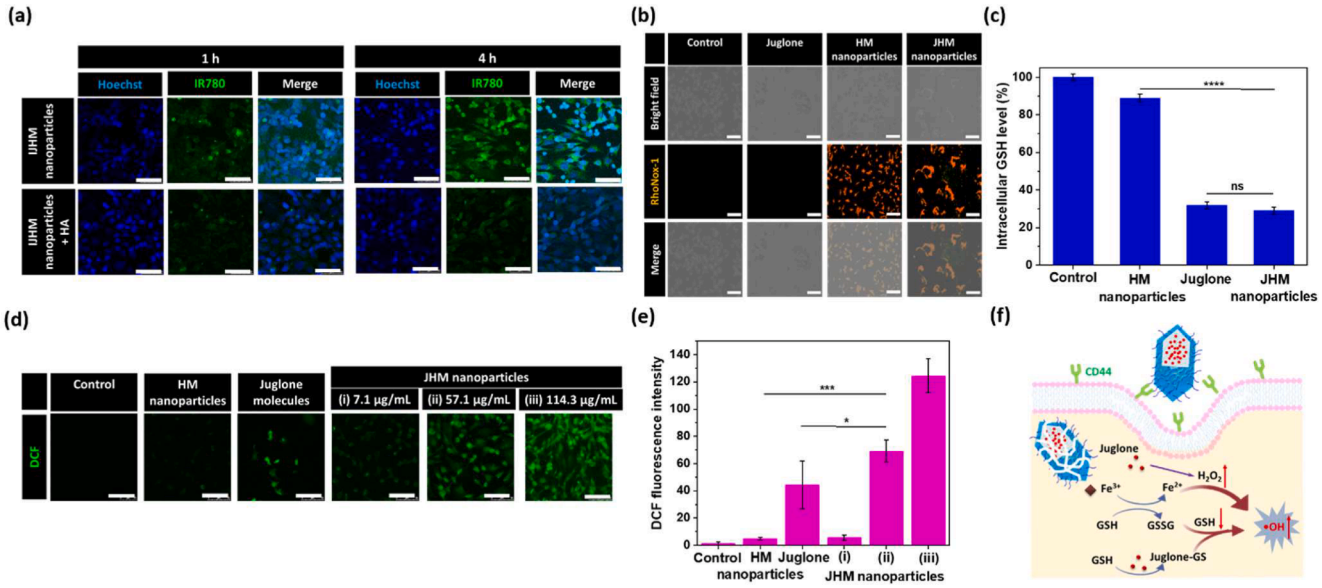

Fig. 4. (a) CLSM images of TRAMP-C1 cells incubated with IJHM nanoparticles or IJHM nanoparticles and free HA segments at 37 °C for 1 h and 4 h. (b) RhoNox-1 staining of TRAMP-C1 cells incubated with juglone, HM nanoparticles, and JHM nanoparticles, respectively, at 37 °C for 1.5 h. Scale bars are 100 μm. (c) Intracellular GSH level of TRAMP-C1 cells receiving HM nanoparticles, juglone, and JHM nanoparticles, respectively, at 37 °C for 6 h. (d) DCF fluorescence images and (e) quantification analysis of TRAMP-C1 cells incubated with different formulations. Scale bars are 50 μm. (f) Schematic illustration of the mechanism of intracellular GSH depletion and •OH generation based on JHM nanoparticles.

Fig. 4c, the intracellular GSH level (ca. 88 %) of TRAMP-C1 cells incubated with HM nanoparticles was somewhat lower than that of cells without any treatment, indicating Fe^{3+}-mediated GSH consumption of HM nanoparticles. Notably, the intracellular GSH level of TRAMP-C1 cells treated with juglone or JHM nanoparticles markedly decreased to below 40 %. These results suggest that the JHM nanoparticles could efficiently scavenge intracellular GSH via the juglone-induced Michael addition and Fe^{3+}-mediated GSH oxidation. Subsequently, the ability of JHM nanoparticles to produce intracellular •OH was assessed using the DCFH-DA assay. No significant DCF fluorescence signal was observed in the TRAMP-C1 cells incubated with HM nanoparticles due to the consumption of •OH by endogenous GSH (Fig. 4d and e). By contrast, TRAMP-C1 cells treated with juglone molecules showed some green DCF fluorescence signals, which is attributed to that juglone molecules could upregulate intracellular H_2O_2 levels. Notably, at prescribed concentrations of HM and juglone (juglone concentration = 20 μg/mL; HM concentration = 37.1 μg/mL), TRAMP-C1 cells treated with JHM nanoparticles exhibited significantly higher DCF fluorescence signals compared to those exposed to either HM nanoparticles or juglone molecules alone. This demonstrates that the juglone-mediated H_2O_2 generation and GSH depletion of JHM nanoparticles can prominently promote Fe^{3+}-driven Fenton/Fenton-like reaction, thus augmenting intracellular •OH generation (Fig. 4f). Moreover, as the concentration of JHM nanoparticles was increased from 7.1 to 114.3 μg/mL, the DCF fluorescence in treated TRAMP-C1 cells was significantly enhanced (Fig. 4d and e), indicating elevated intracellular •OH generation due to more nanoparticle internalization.

3.4. Mitochondrial injury and intracellular LPO production

Several studies suggest that excessive production of •OH can cause oxidative damage to mitochondria, leading to a loss of mitochondrial membrane potential [55,56]. To further verify mitochondrial injury elicited by JHM nanoparticles in TRAMP-C1 cells, the mitochondrial dysfunction was evaluated using the potential-sensitive fluorescent probe JC-1. This probe detects changes in the membrane potential of mitochondria by shifting from red fluorescence (JC-1 aggregates) to green fluorescence (JC-1 monomers). As revealed in Fig. 5a, TRAMP-C1 cells incubated with HM nanoparticles showed visible red fluorescence comparable to the control group, indicating that insufficient •OH

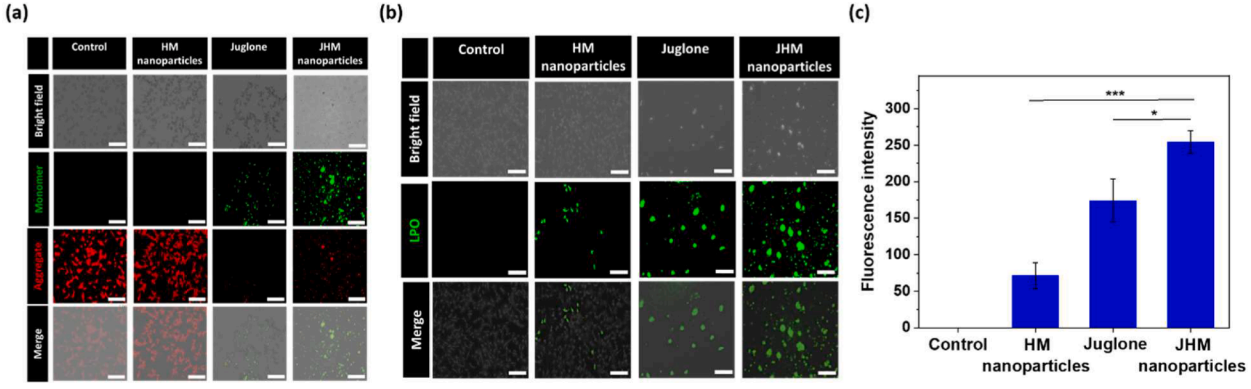

Fig. 5. (a) JC-1 staining of TRAMP-C1 cells treated with juglone molecules, HM nanoparticles, and JHM nanoparticles, respectively, at 37 °C for 1.5 h. (b) BODIPY™581/591 C11 staining and (c) fluorescence intensity of TRAMP-C1 cells receiving different treatments at 37 °C for 1.5 h. Scale bars are 100 μm.

generation of HM nanoparticles within cells cannot destroy mitochondria. Notably, a significant reduction in red fluorescence and an increase in green fluorescence were observed in the TRAMP-C1 cells treated with juglone molecules, reflecting the occurrence of mitochondrial dysfunction. This finding aligns with previous reports indicating that juglone molecules can cause mitochondrial damage by generating ROS and inducing oxidative stress [31]. Importantly, TRAMP-C1 cells treated with JHM nanoparticles exhibited a significant increase in green fluorescence and a decrease in red fluorescence, demonstrating that the JHM nanoparticles could markedly induce oxidative damage to mitochondria by generating large amounts of •OH (Fig. 5a).

Intracellular •OH generation, GSH depletion, and GPX4 downregulation have been demonstrated to provoke LPO accumulation, ultimately triggering ferroptosis [56–58]. Encouraged by the prominent intracellular •OH production and GSH consumption of the JHM nanoparticles, their capability to elicit LPO in TRAMP-C1 cells was evaluated using C11-BODIPY$^{581/591}$, a fluorescent sensor for LPO. Compared to the control group without green fluorescence signals, TRAMP-C1 cells incubated with HM nanoparticles displayed weak green fluorescence (Fig. 5b and c), indicating somewhat raised LPO levels driven by Fe^{3+}-induced •OH generation. The appreciably increased green fluorescence signals were attained in the juglone-treated TRAMP-C1 cells. This suggests that the internalized juglone molecules could lead to LPO via enhanced H_2O_2 production and oxidative stress. Notably, compared to juglone, the JHM nanoparticles largely promoted intracellular LPO levels as reflected by the strong fluorescence of the treated cells. These findings demonstrate that the robust •OH generation and GSH exhaustion mediated by JHM nanoparticles significantly enhance LPO production in TRAMP-C1 cells, thereby initiating ferroptosis.

3.5. In vitro chemo/chemodynamic therapy

To evaluate the anticancer effectiveness of JHM nanoparticles based on the chemodynamic-chemo therapy, we assessed the viability of TRAMP-C1 cells treated with JHM nanoparticles using the MTT assay. As presented in Fig. 6a, the viability of TRAMP-C1 cells incubated with HM nanoparticles somewhat decreased to 81.6 % with increasing nanoparticle concentration to 50 μg/mL, indicating that the single CDT delivered by HM nanoparticles could only slightly suppress TRAMP-C1 cell proliferation due to the significant •OH scavenging by intracellular massive GSH. For the juglone-treated TRAMP-C1 cells, a considerable decrease in cell viability was observed as juglone concentration increased beyond 0.625 μg/mL. This demonstrates that juglone molecules can effectively induce cell death by damaging mitochondria through the upregulated intracellular H_2O_2 levels and oxidative stress, as mentioned above. Moreover, some studies reported that juglone suppressed Pin1 activity to induce cancer cell death [28,32]. Notably, TRAMP-C1 cells treated with JHM nanoparticles showed appreciably declined viability in a concentration-dependent manner compared to cells receiving HM nanoparticles. This suggests that the endocytosed JHM nanoparticles can inhibit cell proliferation via the juglone-based chemotherapy combined with Fe^{3+}/juglone-induced GSH depletion-enhanced CDT. Fluorescence imaging of calcein-AM/PI-stained TRAMP-C1 cells treated with various formulations further confirmed the sound anticancer effects of free juglone molecules and JHM nanoparticles, as well as the minor cytotoxicity of HM nanoparticles (Fig. 6b), consistent with MTT data. Also, TRAMP-C1 cells incubated with JHM nanoparticles displayed enhanced PI staining with increasing JHM nanoparticle concentration, verifying again the concentration-dependent cytotoxicity of JHM nanoparticles. Furthermore, based on the cytotoxicity results (Fig. 6a), the IC_{50} value of JHM nanoparticles was found to be ca 23.8 μg/mL, higher than that (1.25 μg/mL) of free juglone molecules. The lower cytotoxicity observed for JHM nanoparticles compared with free juglone may be explained by the following reasons. First, owing to their small molecular weight and lipophilic naphthoquinone structure, hydrophobic juglone molecules readily enter cells via passive diffusion, whereas JHM nanoparticles are internalized through energy-dependent CD44-mediated endocytosis. Moreover, the internalized JHM nanoparticles gradually release juglone molecules through acidity/GSH-triggered structural disintegration. Although the cytotoxicity of JHM nanoparticles is lower than that of free juglone molecules, it was expected that the JHM nanoparticles could efficiently accumulate in tumor sites through the EPR effect and CD44-targeting capability, increasing localized juglone concentration to amplify the chemo/chemodynamic anticancer effect.

3.6. Biodistribution and tumor deposition

Before evaluating the antitumor effect of the JHM nanoparticle, its hemocompatibility was assessed using a hemolysis assay. As shown in Fig. 7a and b, the hemolysis rate of JHM nanoparticles remained below the permissible limit (2 %) even at a high concentration of 200 μg/mL, demonstrating their good hemocompatibility and suitability for intravenous administration. Due to the poor fluorescence property of JHM nanoparticles, the IJHM nanoparticles were employed to evaluate their tumor deposition and biodistribution using fluorescence imaging. As

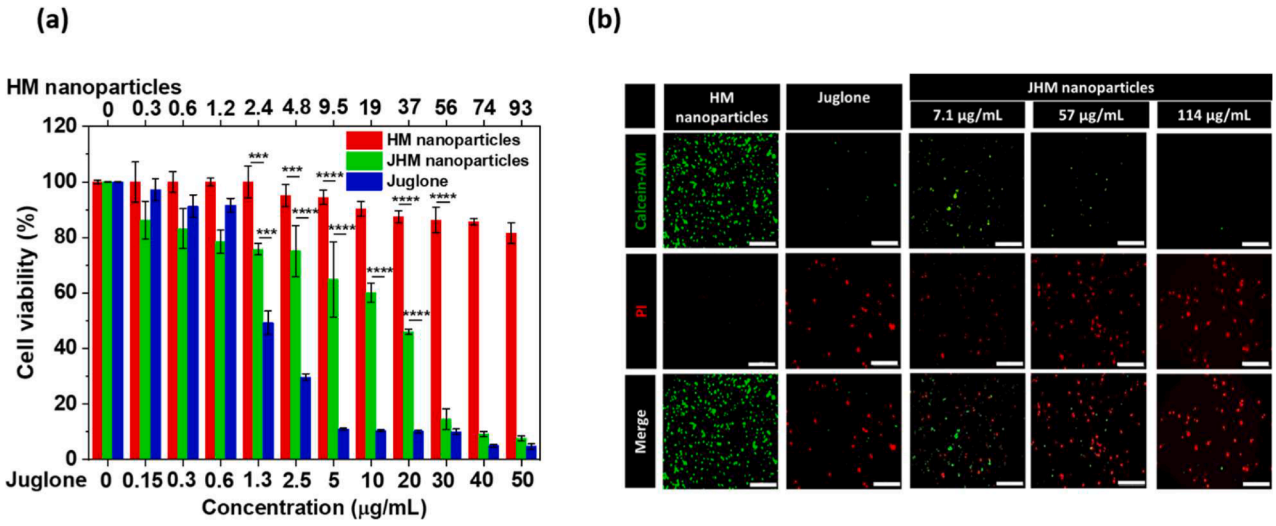

Fig. 6. (a) Cell viability and (b) calcein-AM/PI staining of TRAMP-C1 cells treated with free juglone molecules, HM nanoparticles, and JHM nanoparticles, respectively. Scale bars are 100 μm.

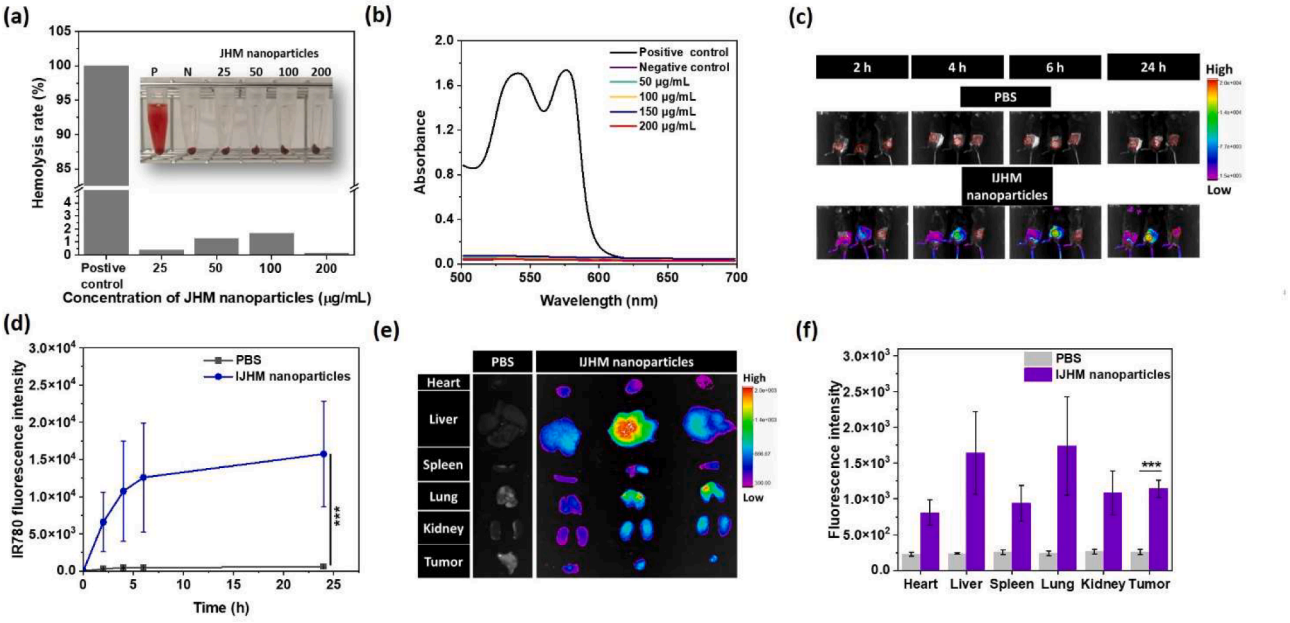

Fig. 7. (a) Digital photos and quantitative analysis of hemolysis of JHM nanoparticles. (b) Absorption spectra of red blood cells treated with deionized water, 0.9 % saline solution, and JHM nanoparticles, respectively. (c) In vivo NIR fluorescence photos and (d) IR780 fluorescence signals of TRAMP-C1 tumor-bearing mice with intravenous injection of PBS as the control, or IJHM nanoparticles ($n = 3$). The tumor regions were labeled with red circles. (e) *Ex vivo* NIR fluorescence images and (f) average IR780 fluorescence intensities of tumors and major organs at 24 h post-injection with PBS and IJHM nanoparticles, respectively. ($n = 3$).

presented in Fig. 7c and d, the tumor sites of TRAMP-C1 tumor-bearing mice ($n = 3$) receiving intravenous injection of IJHM nanoparticles showed gradually enhanced IR780 fluorescence signals over 24 h after injection. Ex vivo analysis also revealed strong fluorescence in tumors treated with IJHM nanoparticles (Fig. 7e, f). These findings demonstrate that JHM nanoparticles can deposit within tumor tissues via the EPR effect and HA-mediated tumor targeting. Moreover, obvious fluorescence signals were observed in the liver, spleen, and lung of mice treated with IJHM nanoparticles, suggesting the inevitable clearance of these nanoparticles by the mononuclear phagocyte system. Similar biodistribution patterns of MOF-based nanoparticles have been reported elsewhere [59,60].

3.7. *In vivo antitumor effect*

Because of the sound tumor accumulation of JHM nanoparticles, their antitumor efficacy was assessed using a TRAMP-C1 tumor-bearing mouse model (Fig. 8a). As shown in Fig. 8b, the TRAMP-C1 tumor-bearing mice receiving HM nanoparticle treatment showed appreciable tumor growth similar to the PBS group, indicating the failure of tumor growth inhibition by the single CDT due to the insufficient •OH generation within tumor regions. For juglone-treated TRAMP-C1 tumor mice, tumor growth was somewhat suppressed, indicating that juglone-mediated chemotherapy only achieved limited tumor inhibition due to a lack of tumor targeting for juglone. Notably, TRAMP-C1 tumor-bearing mice treated with JHM nanoparticles exhibited significantly smaller tumor volumes compared to those treated with PBS, free juglone molecules, or HM nanoparticles alone. Corresponding to the above results, tumors from mice receiving JHM nanoparticles were the smallest in size and weight among all groups (Fig. 8c and d). These results strongly validate that JHM nanoparticles more effectively inhibited tumor growth through the juglone-based chemotherapy combined with dual GSH depletion-augmented chemodynamic therapy compared to either treatment alone.

To further explore the antitumor effects of JHM nanoparticles, after 14-day treatment, the tumors of the mice were collected for H&E, caspase-3, and GPX4 staining. As presented in Fig. 8e, compared to the free juglone and HM nanoparticle groups, which maintained normal cell morphology in much of the tumor tissue, the JHM nanoparticle-treated tumors showed significant changes, with a notable number of necrotic cells. The largest nucleus shrinkage was observed in the JHM nanoparticle group, marked by pronounced vacuolar degeneration of tumor cells. Moreover, caspase-3 staining images revealed that the apoptosis of tumor cells treated with JHM nanoparticles was significantly promoted compared to that of other treatment groups, which corresponded well with the therapeutic outcomes. On the other hand, to further confirm the JHM nanoparticle-elicited ferroptosis, immunohistochemistry analysis of tumor sections for GPX4 (a biomarker of ferroptosis) was performed. As presented in the GPX4-stained images of tumor sections, the JHM nanoparticle group exhibited significantly decreased GPX4 expression compared to the other treatment groups. This demonstrates again that JHM nanoparticles can effectively inhibit GPX4 expression by exhausting GSH of tumor cells via juglone-involved Michael addition and Fe^{3+}-mediated redox reaction. During the treatment process, no significant variation in body weight was observed in all treatment groups (Fig. 8f), indicating that the JHM nanoparticles did not elicit serious acute toxicity. Moreover, as shown in the H&E staining images of major organs of mice receiving different treatments (Fig. S7), the JHM nanoparticle group exhibited little tissue histological damage and abnormality, similar to the PBS group, revealing good in vivo biocompatibility and biosafety. Based on the above findings, the tumor-targeting JHM nanoparticles developed herein integrated juglone chemotherapy with dual GSH depletion-enhanced CDT, thereby provoking apoptosis and ferroptosis to inhibit prostate tumor growth effectively (Scheme 1b), and maintained sound biosafety.

4. Conclusions

In this work, the JHM nanoparticles were fabricated to realize tumor-targeted chemodynamic-chemo therapy for effective treatment of prostate cancer. The resulting JHM nanoparticles exhibited several prominent properties, including (1) sufficient juglone payload, (2) sound dispersion in serum-containing milieu, (3) acidity/GSH-enhanced juglone and Fe^{3+} liberation, (4) Fe^{3+}/juglone-mediated GSH depletion,

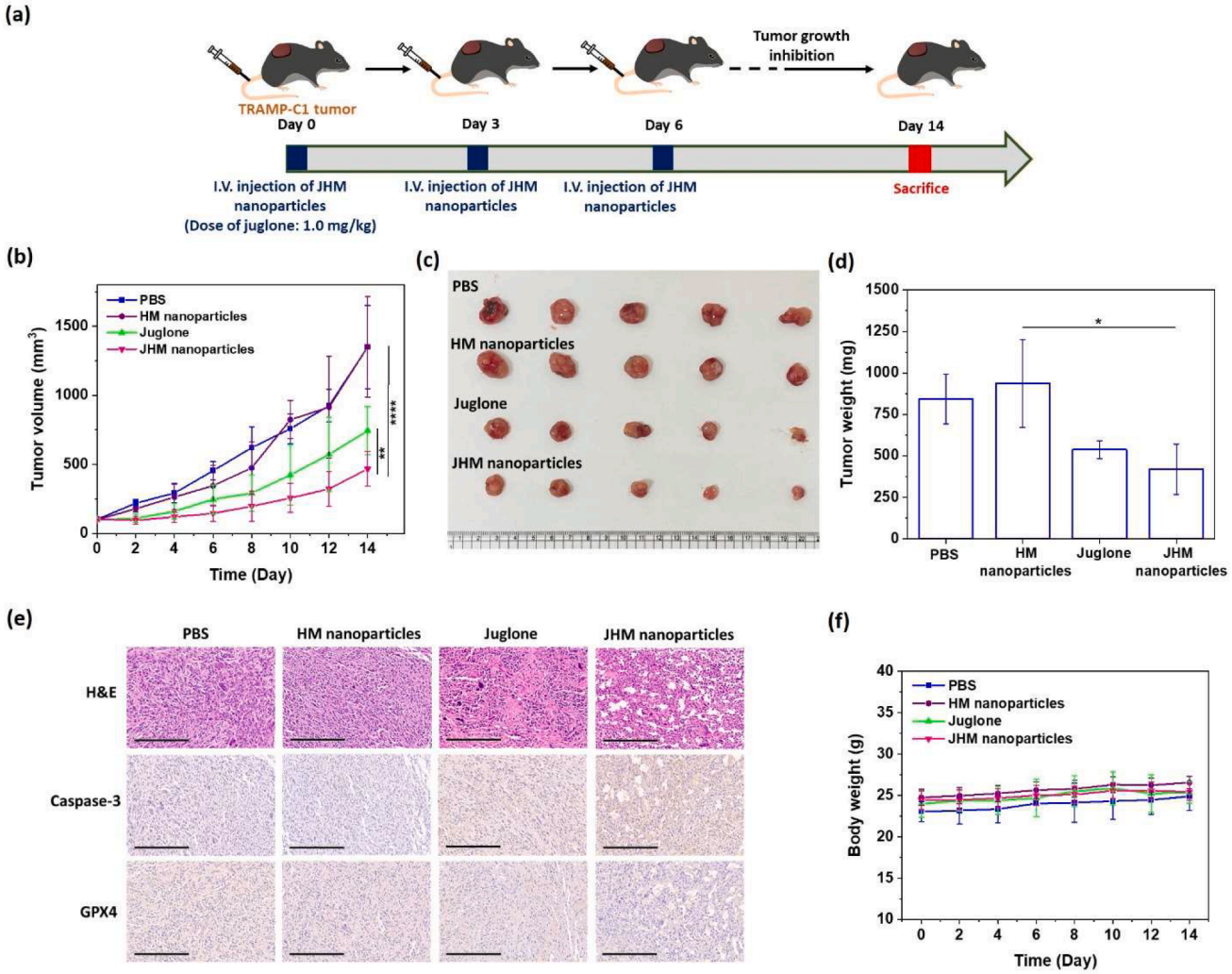

Fig. 8. (a) Schematic diagram of in vivo therapeutic evaluation in the TRAMP-C1 tumor-bearing mice. (b) Tumor volume profiles during the treatment. (c) Digital photos and (d) weights of the tumors collected from the euthanized mice after 14 days of treatment ($n = 5$). (e) Histological analysis of tumor: Staining images of H&E, caspase-3, and immunohistochemistry of GPX4 in tumor tissues receiving various treatments. (f) Body weight profiles of TRAMP-C1 tumor-bearing mice subjected to different treatments.

(5) good hemocompatibility, and (6) active tumor targeting. Through CD44-mediated internalization, the efficient uptake of JHM nanoparticles by TRAMP-C1 cells was achieved. Also, the JHM nanoparticles effectively depleted intracellular GSH via Fe^{3+}/Fe^{2+} redox couple combined with juglone-based Michael addition, and degraded endogenous H_2O_2 into •OH, thus inducing cell apoptosis and ferroptosis upon augmented LPO and mitochondrial damage. Furthermore, compared to juglone molecules and HM nanoparticles, the JHM nanoparticles potently inhibited TRAMP-C1 tumor growth in vivo by chemodynamic-chemo combination therapy without acute adverse effects. Collectively, the rational design of JHM nanoparticles provided a promising strategy for effective prostate tumor-targeted chemodynamic-chemo therapy.

Data availability

Any data from this study will be available from the corresponding author on request.

Funding

This work is supported by the National Science and Technology Council (NSTC 113–2628-E-005–002-MY3, NSTC 113–2622-E-005–017), Taiwan.

CRediT authorship contribution statement

Yi-Ting Yeh: Validation, Project administration, Methodology, Investigation, Formal analysis, Conceptualization. **Wei-Jen Hsu:** Visualization, Validation, Methodology, Investigation, Formal analysis. **Tzu-Chen Lin:** Validation, Methodology, Investigation, Formal analysis, Conceptualization. **Ching-Ju Huang:** Methodology, Investigation, Formal analysis. **I-Ju Liu:** Visualization, Resources, Methodology, Formal analysis. **Shang-Hsiu Hu:** Resources, Investigation, Conceptualization. **De-Wei Lai:** Writing – original draft, Supervision, Resources, Methodology, Investigation. **Wen-Hsuan Chiang:** Writing – review & editing, Writing – original draft, Supervision, Methodology, Investigation, Funding acquisition, Conceptualization.

Declaration of competing interest

The authors declare that they have no known competing financial interests or personal relationships that could have appeared to influence the work reported in this paper.

Acknowledgements

We thank the Instrument Center of National Chung Hsing University

for help with measurements of XPS, TEM, SEM, and XRD.

Supplementary materials

Supplementary material associated with this article can be found, in the online version, at doi:10.1016/j.jtice.2026.106665.

References

[1] Cao C, Wang X, Yang N, Song X, Dong X. Recent advances of cancer chemodynamic therapy based on Fenton/Fenton-like chemistry. Chem Sci 2021;13:863–89.
[2] Gao H, Cao Z, Liu H, Chen L, Bai Y, Wu Q, Yu X, Wei W, Wang M. Multifunctional nanomedicines-enabled chemodynamic-synergized multimodal tumor therapy via Fenton and Fenton-like reactions. Theranostics 2023;13:1974–2014.
[3] Asif K, Rahman MM, Canzonieri V, Caligiuri I, Rizzolio F, Adeel M. Self-targeted nanosystem for enhanced chemodynamic cancer therapy. Biomater Sci 2025;13:2320–31.
[4] Hao JN, Ge K, Chen G, Dai B, Li Y. Strategies to engineer various nanocarrier-based hybrid catalysts for enhanced chemodynamic cancer therapy. Chem Soc Rev 2023;52:7707–36.
[5] Sun D, Sun X, Zhang X, Wu J, Shi X, Sun J, Luo C, He Z, Zhang S. Emerging chemodynamic nanotherapeutics for cancer treatment. Adv Heal Mater 2024;13:e2400809.
[6] Liang KA, Chih HY, Liu IJ, Yeh NT, Hsu TC, Chin HY, Tzang BS, Chiang WH. Tumor-targeted delivery of hyaluronic acid/polydopamine-coated Fe^{2+}-doped nano-scaled metal-organic frameworks with doxorubicin payload for glutathione depletion-amplified chemodynamic-chemo cancer therapy. J Colloid Interface Sci 2025;677:400–15.
[7] Deng H, Zhang J, Yang Y, Yang J, Wei Y, Ma S, Shen Q. Chemodynamic and photothermal combination therapy based on dual-modified metal-organic framework for inducing tumor ferroptosis/pyroptosis. ACS Appl Mater Interfaces 2022;14:24089–101.
[8] Chen J, Wang Y, Niu H, Wang Y, Wu A, Shu C, Zhu Y, Bian Y, Lin K. Metal-organic framework-based nanoagents for effective tumor therapy by dual dynamics-amplified oxidative stress. ACS Appl Mater Interfaces 2021;13:45201–13.
[9] Zhu XY, Wang TY, Jia HR, Wu SY, Gao CZ, Li YH, Zhang X, Shan BH, Wu FG. A ferroptosis-reinforced nanocatalyst enhances chemodynamic therapy through dual H_2O_2 production and oxidative stress amplification. J Control Release 2024;367:892–904.
[10] Wu X, Bai Z, Wang H, Wang H, Hou D, Xu Y, Wo G, Cheng H, Sun D, Tao W. CRISPR-Cas9 gene editing strengthens cuproptosis/chemodynamic/ferroptosis synergistic cancer therapy. Acta Pharm Sin B 2024;14:4059–72.
[11] Lin TC, Liu IJ, Chih HY, Tzang BS, Liang JA, Kuo CW, Hung CY, Hsu TC, Chiang WH. Photothermal-enhanced ROS storm by hyaluronic acid-conjugated nanocatalysts to amplify tumor-specific photo-chemodynamic therapy and immune response. Int J Biol Macromol 2025;309:142975.
[12] Kudarha R, Dhas N, Mutalik S. Distinct features of iron based metal organic frameworks (MOFs) for ferroptosis mediated cancer therapy: a comprehensive review. Coord Chem Rev 2023;494:215330.
[13] Hu X, Shen Z, Hao H, Ma K, Zhen A, Yang Y, Liang K, Chen Z, Li J, Lv Y, Chao S, Pei Y, Qu Z, Pei Z. NIR II light-driven nanomotor synergistically enhances immunogenic cell death through photothermal and chemodynamic therapy for melanoma immunotherapy. J Colloid Interface Sci 2025;694:137688.
[14] Jin W, Chen Z, Wang Y, Li J, Li J, Pei Y, Pei Z. Nano metal-photosensitizer based on Aza-BODIPY-Cu complex for CDT-enhanced dual phototherapy. Chin Chem Lett 2024;35:109328.
[15] Wang Y, Chen Z, Li J, Wen Y, Li J, Lv Y, Pei Z, Pei Y. A paramagnetic metal-organic framework enhances mild magnetic hyperthermia therapy by downregulating heat shock proteins and promoting ferroptosis via aggravation of two-way regulated redox dyshomeostasis. Adv Sci 2024;11:2306178.
[16] Yu W, Jia F, Fu J, Chen Y, Huang Y, Jin Q, Wang Y, Ji J. Enhanced transcutaneous chemodynamic therapy for melanoma treatment through cascaded Fenton-like reactions and nitric oxide delivery. ACS Nano 2023;17:15713–23.
[17] Tian Q, Xue F, Wang Y, Cheng Y, An L, Yang S, Chen X, Huang G. Recent advances in enhanced chemodynamic therapy strategies. Nano Today 2021;39:101162.
[18] Zhou Y, Fan S, Feng L, Huang X, Chen X. Manipulating intratumoral Fenton chemistry for enhanced chemodynamic and chemodynamic-synergized multimodal therapy. Adv Mater 2021;33:2104223.
[19] Hu H, Liu X, Hong J, Ye N, Xiao C, Wang J, Li Z, Xu D. Mesoporous polydopamine-based multifunctional nanoparticles for enhanced cancer phototherapy. J Colloid Interface Sci 2022;612:246–60.
[20] Liu Z, Liu S, Liu B, Bian Y, Yuan M, Yang C, Meng Q, Chen C, Ma P, Lin J. Fe(III)-naphthazarin metal-phenolic networks for glutathione-depleting enhanced ferroptosis-apoptosis combined cancer therapy. Small 2023;19:e2207825.
[21] Niu B, Liao K, Zhou Y, Wen T, Quan G, Pan X, Wu C. Application of glutathione depletion in cancer therapy: enhanced ROS-based therapy, ferroptosis, and chemotherapy. Biomaterials 2021;277:121110.
[22] Zhao F, Yu H, Wang C, Xu J, Gao H, Ying Y, Li W, Li J, Zheng J, Qiao L, Che S, Yu J. Copper/iron bimetal phenolic networks boosted apoptosis/ferroptosis/cuproptosis combined tumor therapy through dual glutathione depletion. Chem Eng J 2024;500:157408.
[23] Chen W, Hu F, Gao Q, Zheng C, Bai Q, Liu J, Sun N, Zhang W, Zhang Y, Dong K, Lu T. Tumor acidification and GSH depletion by bimetallic composite nanoparticles for enhanced chemodynamic therapy of TNBC. J Nanobiotechnology 2024;22:98.
[24] Wang TH, Shen MY, Yeh NT, Chen YH, Hsu TC, Chin HY, Wu YT, Tzang BS, Chiang WH. Photothermal nanozymes to self-augment combination cancer therapy by dual-glutathione depletion and hyperthermia/acidity-activated hydroxyl radical generation. J Colloid Interface Sci 2023;650:1698–714.
[25] Liu J, Yuan Y, Cheng Y, Fu D, Chen Z, Wang Y, Zhang L, Yao C, Shi L, Li M, Zhou C, Zou M, Wang G, Wang L, Wang Z. Copper-based metal-organic framework overcomes cancer chemoresistance through systemically disrupting dynamically balanced cellular redox homeostasis. J Am Chem Soc 2022;144:4799–809.
[26] Wang J, Liu K, Wang XF, Sun DJ. Juglone reduces growth and migration of U251 glioblastoma cells and disrupts angiogenesis. Oncol Rep 2017;38:1959–66.
[27] Du J, Krishnamoorthy K, Ramabhai V, Yang D. Targeting ferroptosis as a therapeutic implication in lung cancer treatment by a novel naphthoquinone inducer: juglone. Mol Biotechnol 2024;66:1071–81.
[28] Zhao L, Li Z, Wei J, Xiao Y, She Y, Su Q, Zhao T, Li J, Shao J. Juglone-loaded metal-organic frameworks for H_2O_2 self-modulating enhancing chemodynamic therapy against prostate cancer. Chem Eng J 2022;430:133057.
[29] Dong YT, Jin Q, Zhou L, Chen J. N-heterocyclic carbene catalyzed sulfenylation of α,β-unsaturated aldehydes. Org Lett 2016;18:5708–11.
[30] Böhme A, Thaens D, Schramm F, Paschke A, Schüürmann G. Thiol reactivity and its impact on the ciliate toxicity of α,β-unsaturated aldehydes, ketones, and esters. Chem Res Toxicol 2010;23:1905–12.
[31] Liu Z, Liu S, Liu B, Meng Q, Yuan M, Yang C, Bian Y, Ma P, Lin J. Fe(III)-juglone nanoscale coordination polymers for cascade chemodynamic therapy through synergistic ferroptosis and apoptosis strategy. Chin Chem Lett 2024;35:109626.
[32] Ahmad T, Suzuki YJ. Juglone in oxidative stress and cell signaling. Antioxid (Basel) 2019;8:91.
[33] Li XN, Tang QY, Tang MC, Deng HR, Hu K, Pan LF, Wang SB, Li B, Kong XD. A magnetic nanoreactor with microenvironment regulation capability for targeted and enhanced tumor chemodynamic therapy. Chem Eng J 2025;509:161356.
[34] Shah VM, Rizvi S, Smith A, Tsuda M, Krieger M, Pelz C, MacPherson K, Eng J, Chin K, Munks MW, Daniel CJ, Al-Fatease A, Yardimci GG, Langer EM, Brody JR, Sheppard BC, Alani AW, Sears RC. Micelle-formulated juglone effectively targets pancreatic cancer and remodels the tumor microenvironment. Pharmaceutics 2023;15:2651.
[35] Zoubi WA, Park N. Orbital modulation in high-entropy alloy catalysts: an effective strategy for enhancing catalytic performance. Chem Commun 2025;61:18590–607.
[36] Zoubi WA, Alnaasan M, Assfour B, Leoni S, Hussain I, Kim S, Ko YG. Totally defined nanocatalysis: detection of polyelement nanoparticles by deep learning. InfoMat 2025;7:e70009.
[37] Hazmatulhaq F, Sheng Y, Suhartono T, Saad AM, Salsabila S, Assfour B, Zoubi WA, Ko YG. Layer-by-layer growth of organic molecules controlled by the defective inorganic surface for enhanced corrosion protection and bioactivity properties of magnesium alloy. EcoMat 2025;7:e70005.
[38] Wu L, Liu Y, Shi T, Liu Z, Zhang R, Chen J. Bimetallic MOFs-derived CuS/FeMn-C composite materials efficiently activate persulfate for catalytic degradation of ciprofloxacin. J Taiwan Inst Chem Eng 2025;174:106236.
[39] Abdulkadir BA, Setiabudi HD. Bibliometric insights into metal-organic frameworks modified with metal-based materials for hydrogen storage: prospects, opportunities and challenges. J Taiwan Inst Chem Eng 2025;167:105893.
[40] Soleimani B, Shahrak MN, Walton KS. The influence of different functional groups on enhancing CO_2 capture in metal-organic framework adsorbents. J Taiwan Inst Chem Eng 2024;163:105638.
[41] Pattappan D, Liao CJ, Kumar RS, Ramesh S, Kumar RTR, Yang W, Haldorai Y, Lai YT. Rational design of amine-terminated terephthalate in bismuth metal-organic framework for boosting sunlight-catalytic removal of organic pollutants. J Taiwan Inst Chem Eng 2024;165:105725.
[42] Pooresmaeil M, Hassan Namazi H. Metal-organic framework/carboxymethyl starch/graphene quantum dots ternary hybrid as a pH sensitive anticancer drug carrier for co-delivery of curcumin and doxorubicin. J Taiwan Inst Chem Eng 2022;141:104573.
[43] Qiao C, Zhang R, Wang Y, Jia Q, Wang X, Yang Z, Xue T, Ji R, Cui X, Wang Z. Rabies virus-inspired metal-organic frameworks (MOFs) for targeted imaging and chemotherapy of glioma. Angew Chem Int Ed Engl 2020;59:16982–8.
[44] Xu B, Yang H, Cai Y, Yang H, Li C. Preparation and photocatalytic property of spindle-like MIL-88B(Fe) nanoparticles. Inorg Chem Commun 2016;67:29–31.
[45] Di X, Pei Z, Pei Y, James TD. Tumormicroenvironment-oriented MOFs for chemodynamic therapy. Coord Chem Rev 2023;484:215098.
[46] Wang D, Zhou J, Chen R, Shi R, Xia G, Zhou S, Liu Z, Zhang N, Wang H, Guo Z, Chen Q. Magnetically guided delivery of DHA and Fe ions for enhanced cancer therapy based on pH-responsive degradation of DHA-loaded Fe_3O_4@C@MIL-100(Fe) nanoparticles. Biomaterials 2016;107:88–101.
[47] Yeh NT, Lin TC, Liu IJ, Hu SH, Hsu TC, Chin HY, Tzang BS, Chiang WH. Hyaluronic acid-covered ferric ion-rich nanobullets with high zoledronic acid payload for breast tumor-targeted chemo/chemodynamic therapy. Int J Biol Macromol 2024;279:135271.
[48] Wen Y, Qiu Q, Feng F, Zhu Y, Zhang J, Sun Z, Zhang T, Shi W, Shi J. Tailored biomimetic nanoreactor improves glioma chemodynamic treatment via triple glutathione depletion and prompt acidity elevation. Mater Today Bio 2025;30:101447.
[49] Yang XX, Xu X, Wang MF, Xu HZ, Peng XC, Han N, Yu TT, Li LG, Li QR, Chen X, Wen Y, Li TF. A nanoreactor boosts chemodynamic therapy and ferroptosis for synergistic cancer therapy using molecular amplifier dihydroartemisinin. J Nanobiotechnology 2022;20:230.

[50] Wang YY, Zhang XY, Li SL, Jiang FL, Jiang P, Liu Y. AuPt-loaded Cu-doped polydopamine nanocomposites with multienzyme-mimic activities for dual-modal imaging-guided and cuproptosis-enhanced photothermal/nanocatalytic therapy. Anal Chem 2023;95:14025–35.
[51] Qin X, Xiao J, Li H, Huang H, Jin H, Zhang Y, Tian G, Wang G, Zhang G. Copper-based inorganic nanozymes enhance the electrical conductivity of tumors to synergistically induce the pyroptosis, ferroptosis, and apoptosis of tumors. Inorg Chem Front 2023;10:7176–86.
[52] Xiao Z, Zuo W, Chen L, Wu L, Liu N, Liu J, Jin Q, Zhao Y, Zhu X. H2O2 self-supplying and GSH-depleting nanoplatform for chemodynamic therapy synergetic photothermal/chemotherapy. ACS Appl Mater Interfaces 2021;13:43925–36.
[53] Pei Y, Liu M, He C, Chen H, Li J, Zhang L, Zhang M, Choie MMF, Jia H, Bian W. Application of pH and hyaluronidase dual-responsive mesoporous carbon nitride nano-drug delivery system for chemodynamic therapy and chemotherapy combination therapy of non-small cell lung cancer. Appl Mater Today 2024;41:102469.
[54] Matějková N, Korecká L, Šálek P, Kočková O, Pavlova E, Kašparová J, Obořilová R, Farka Z, Frolich K, Adam M, Carrillo A, Šinkorová Z, Bílková Z. Hyaluronic acid nanoparticles with parameters required for in vivo applications: from synthesis to parametrization. Biomacromolecules 2024;25:4934–45.
[55] Song WF, Zeng JY, Ji P, Han ZY, Sun YX, Zhang XZ. Self-assembled copper-based nanoparticles for glutathione activated and enzymatic cascade-enhanced ferroptosis and immunotherapy in cancer treatment. Small 2023;19:e2301148.
[56] Cun JE, Pan Y, Zhang Z, Lu Y, Li J, Pan Q, Gao W, Luo K, He B, Pu Y. Photo-enhanced upcycling H_2O_2 into hydroxyl radicals by IR780-embedded Fe_3O_4@MIL-100 for intense nanocatalytic tumor therapy. Biomaterials 2022;287:121687.
[57] Li Y, Fan W, Gu X, Liu S, He T, Gou S, Meng W, Li M, Liu X, Ren Y, Qi C, Ca K. Biodegradable ferric phosphate nanocarriers with tumor-specific activation and glutathione depletion for tumor self-enhanced ferroptosis and chemotherapy. Adv Funct Mater 2024;34:2313540.
[58] Zhu XY, Wang TY, Jia HR, Wu SY, Gao CZ, Li YH, Zhang X, Shan BH, Wu FG. A ferroptosis-reinforced nanocatalyst enhances chemodynamic therapy through dual H_2O_2 production and oxidative stress amplification. J Control Release 2024;367:892–904.
[59] Cheng R, Jiang L, Gao H, Liu Z, Mäkilä E, Wang S, Saiding Q, Xiang L, Tang X, Shi M, Liu J, Pang L, Salonen J, Hirvonen J, Zhang H, Cui W, Shen B, Santos HA. A pH-responsive cluster metal-organic framework nanoparticle for enhanced tumor accumulation and antitumor effect. Adv Mater 2022;34:e2203915.
[60] Ni W, Wu J, Fang H, Feng Y, Hu Y, Lin L, Chen J, Chen F, Tian H. Photothermal-chemotherapy enhancing tumor immunotherapy by multifunctional metal-organic framework based drug delivery system. Nano Lett 2021;21:7796–805.